ELSEVIER

International Journal of Heat and Fluid Flow 23 (2002) 298–307

International Journal of HEAT AND FLUID FLOW

www.elsevier.com/locate/ijhff

Modelling of transport phenomena in laser surface alloying with distributed species mass source ☆

P. Mohan Raj [a], S. Sarkar [a], S. Chakraborty [a], G. Phanikumar [b], P. Dutta [a,*], K. Chattopadhyay [b]

[a] *Department of Mechanical Engineering, Indian Institute of Science, Bangalore 560012, India*
[b] *Department of Metallurgy, Indian Institute of Science, Bangalore 560012, India*

Abstract

In this paper, a three-dimensional transient macroscopic numerical model is developed for the description of transport phenomena during laser surface alloying. In order to make accurate estimates for the species composition distribution during the process, the addition of alloying elements is formulated by devising a species generation term for the solute transport equation. By employing a particle-tracking algorithm and a simultaneous particle-melting consideration, the species source term is estimated by the amount of fusion of a spherical particle as it passes through a particular control volume. Numerical simulations are performed for two cases. The first case corresponds to aluminium as alloying element on a nickel substrate, while the second case is for alloying nickel on aluminium substrate. It is observed for the latter case that the melting of the alloying element is not instantaneous, and hence it cannot be modelled as a species mass flux boundary condition at the top surface. The predicted results are compared with experiments, and the agreement is found to be good. © 2002 Published by Elsevier Science Inc.

Keywords: Laser surface alloying; Computational modelling; Aluminium; Nickel

1. Introduction

Laser surface alloying is generally used to improve hardness, wear as well as corrosion resistance, and some other surface characteristics of individual products. Fig. 1 shows a schematic diagram of a typical laser surface alloying process. As shown in the figure, a laser beam moving with a constant scanning speed in the horizontal direction and having a defined power distribution strikes the surface of an opaque material, and a part of the energy is absorbed. A thin melt pool forms on the surface due to laser heating. Simultaneously, a powder of a different material is fed into the pool, which mixes with the molten substrate by convection and diffusion. As the laser source moves away from a location, resolidification of the zone occurs, leading to a final microstructure of the alloyed surface.

During laser surface alloying, as the heat source interacts with the molten substrate, several complex phenomena such as melting, Marangoni convection, mixing of the powder feed, alloy solidification, and resulting microstructural evolution occur. In this context, it would be desirable to develop a reliable computational model that can simulate the entire physical process including heating, melting, convection, mixing, and solidification. The model may be used to link the process parameters with the final microstructure and properties of the alloyed region.

Although there have been several previous numerical studies on laser melting (Chan et al., 1984, 1987, 1988; Basu and Srinivasan, 1988; Kou and Wang, 1986; Chen and Huang, 1990; He et al., 1995), there have been relatively few studies (notably that of He et al. (1995)) on laser surface alloying in which species addition and mass transport was also taken into account. In the work of He et al. (1995), a two-dimensional quasi-steady model was used to model the laser surface alloying process. The alloying element was assumed to be introduced on the pool surface in a fully molten state. This was modelled

☆ This paper is a revised and expanded version of a paper presented at CHT'01, the Second International Symposium on Advances in Computational Heat Transfer (Palm Cove, Qld., Australia, 20–25 May 2001), the proceedings of which were published by Begell House, Inc.

* Corresponding author. Tel.: +91-3600411x2332; fax: +91-80-360-0648.

E-mail address: pradip@mecheng.iisc.ernet.in (P. Dutta).

0142-727X/02/$ - see front matter © 2002 Published by Elsevier Science Inc.
PII: S0142-727X(02)00177-7

Nomenclature

a	a large number
a_p, a_p^0	discretisation equation coefficients
b	small number to avoid division by zero
c	specific heat
C	concentration
D	species mass diffusion coefficient
f_l	liquid fraction of the solute
F^{-1}	inverse of latent heat function
g	acceleration due to gravity
h	convective heat transfer coefficient
h_s	sensible enthalpy
H	total enthalpy
k	thermal conductivity
k_p	partition coefficient
L	latent heat of fusion
m_f	powder feed rate
$\dot{m}$	mass flux
n	normal direction
p	pressure
q''	heat flux
Q	net energy input
r	distance from laser centreline
r_q	radius of heat input
R	radial distance from centre of particle
S	source term
S_{gen}	species source term generated in a control volume
T	temperature
t	time
u	x-component of velocity
u_{scan}	laser scanning velocity
v	y-component of velocity
v_n	interface velocity
w	z-component of velocity
x'	x-coordinate in a fixed frame of reference
x,y,z	coordinates fixed to the laser source

Greeks

β_T	coefficient of volumetric expansion of heat
β_C	coefficient of volumetric expansion of solute
η	efficiency
Γ	diffusion coefficient in general transport equation
ΔV	volume of a computational cell
ΔH	latent enthalpy
ε	emissivity
ϕ	general scalar variable
λ	relaxation factor
σ	surface tension
σ_e	Stefan–Boltzman constant
ρ	density
μ	viscosity

Subscripts

Al	aluminium
Ni	nickel
cv	control volume
max	maximum value
l	liquid
m	melting point
n	iteration level/normal direction
old	old iteration value
p	nodal coefficient
ref	reference

numerically as a mass flux boundary condition at the pool surface. This boundary condition is generally appropriate when the melting point of the alloying material is much lower than that of the substrate (such as Al on Ni). However, this model may not work for the opposite case when the melting point of the alloying material is higher than that of the substrate (such as Ni on Al). In the latter situation, an alloying particle will melt only within that region of the pool where it experiences a temperature higher than its melting point. The particle, instead of melting completely on the pool surface, may melt progressively as it is convected within the pool, thus resulting in a distributed species mass source within the pool.

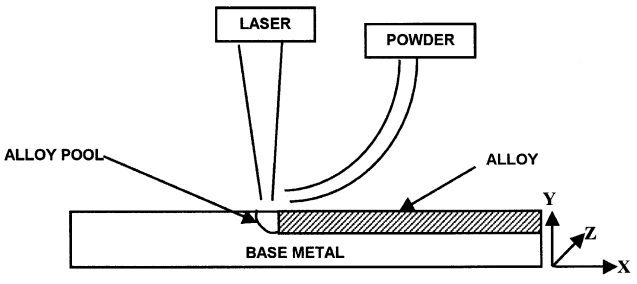

Fig. 1. Schematic of laser surface alloying process setup.

The aim of the present work is to model a laser surface alloying process with a distributed species mass source term. First, the velocity and temperature fields are obtained by the solution of three-dimensional transient mass, momentum and energy conservation equations. Next, the melting of an alloying particle is modelled as it is advected within the pool. The molten mass at any location forms the species mass source at that location, which leads to a distributed species mass source in the melt pool. Finally, the species conservation

equation is solved using the above velocity field and above distributed mass source. The model is first tested for the case of alloying aluminium on a nickel substrate, which corresponds to the case of an alloying element with a melting temperature lower than that of the substrate. Subsequently, the model is applied to the case of alloying nickel on an aluminium substrate, resembling a case of higher melting point alloying element on a lower melting point substrate. For both the above cases, the numerical results of final species distribution in the solidified alloy are compared with corresponding experimental results. The results of the latter case are also compared with those produced by the conventional model that assumes instantaneous melting of alloying element on the top surface.

2. Mathematical and numerical modelling

2.1. Model description

The entire modelling consists of four parts. The first part consists of solution of three-dimensional mass, momentum and energy conservation equations to obtain the velocity and temperature fields. This velocity field is used in the second part of the model, which involves tracking of alloying particles (in a Lagrangian frame) as it is advected within the pool. The third part of the model calculates the progressive melting of each particle as it is advected within the pool, using the temperature field (obtained from first part of model) as a boundary temperature of the particle. Finally, the species conservation equation is solved using the above velocity field and above distributed mass source. The entire procedure is summarised in a flow chart as shown in Fig. 2.

2.1.1. Solution of the velocity and temperature fields

The governing equations for mass, momentum, energy and species transport can be cast in a general conservative form as:

$$\frac{\partial(\rho\phi)}{\partial t}+\nabla\cdot(\rho\vec{u}\phi)=\nabla\cdot(\Gamma\nabla\phi)+S \tag{1}$$

where ϕ is a general scalar variable. Eq. (1) is written with respect to a stationary coordinate system ($x'-y-z$). However, the problem is more conveniently studied in a reference frame fixed with the laser (x–y–z). To achieve this purpose, following transformation can be used:

$$x=x'-u_{\text{scan}}t \tag{2}$$

Using the transformation, the governing equations in moving coordinate system are written as:

$$\text{Continuity}: \quad \nabla\cdot\vec{u}=0 \tag{3}$$

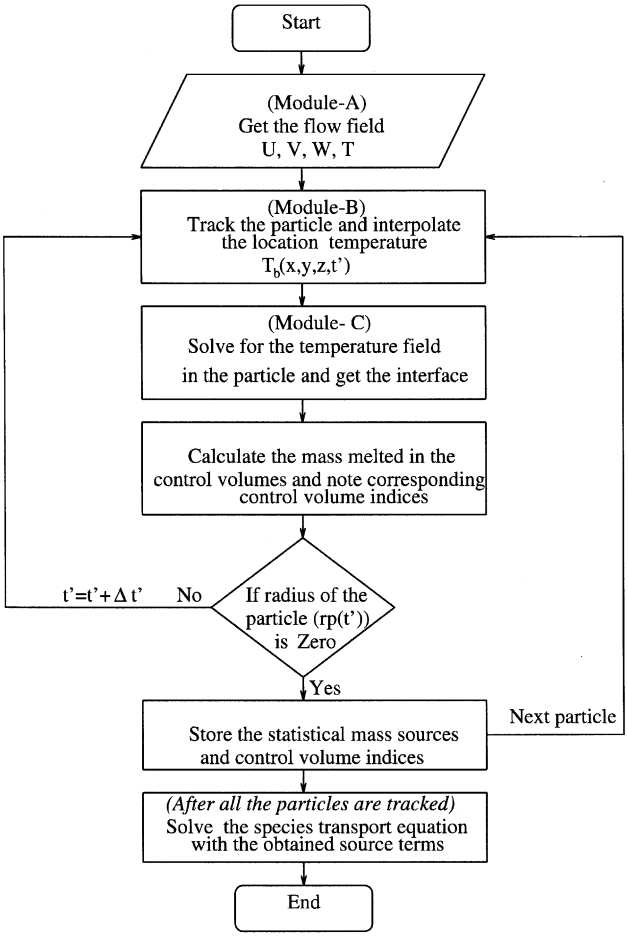

Fig. 2. Flow chart to show stages of modelling.

$$x\text{-momentum}: \quad \frac{\partial(\rho u)}{\partial t}+\nabla\cdot(\rho\vec{u}u)=-\frac{\partial p}{\partial x}+\nabla\cdot(\mu\nabla u)-Au+\frac{\partial(\rho u_{\text{scan}}u)}{\partial x} \tag{4}$$

$$y\text{-momentum}: \quad \frac{\partial(\rho v)}{\partial t}+\nabla\cdot(\rho\vec{u}v)=-\frac{\partial p}{\partial y}+\nabla\cdot(\mu\nabla v)-Av+\frac{\partial(\rho u_{\text{scan}}v)}{\partial x}+\rho g\beta_{\text{T}}(T-T_{\text{ref}})+\rho g\beta_{\text{c}}(C-C_{\text{ref}}) \tag{5}$$

$$z\text{-momentum}: \quad \frac{\partial(\rho w)}{\partial t}+\nabla\cdot(\rho\vec{u}w)=-\frac{\partial p}{\partial z}+\nabla\cdot(\mu\nabla w)-Aw+\frac{\partial(\rho u_{\text{scan}}w)}{\partial x} \tag{6}$$

$$\text{Energy conservation}: \quad \frac{\partial(\rho T)}{\partial t}+\nabla\cdot(\rho\vec{u}T)=\nabla\cdot\left(\frac{k}{c}\nabla T\right)-\frac{1}{c}\frac{\partial}{\partial t}(\rho\Delta H)-\nabla\cdot\left(\frac{\rho}{c}\vec{u}\Delta H\right)-\frac{\partial}{\partial x}\left(\rho u_{\text{scan}}\left(T+\frac{\Delta H}{c}\right)\right) \tag{7}$$

where ΔH represents the latent enthalpy.

In the above formulation, a single-domain enthalpy-porosity approach is employed, in which the solid/liquid interface comes out as a part of the solution, and need not be tracked separately. However, to achieve that purpose additional source terms are to be defined in the momentum equations (terms containing the coefficient 'A'), which ensure a smooth transition of velocity from a zero value at the solid state to an appropriate value at the fully liquid state (Brent et al., 1988). In the present study, we use a modified Darcy's model (Morvan et al., 1999) as described subsequently.

$$A = \frac{\mu_l \rho}{K \rho_l} \tag{8}$$

where K is the permeability. For appropriate modelling of the above term, K has to be properly prescribed as a function of liquid fraction. For that purpose, the Carman–Kozeny relation (Brent et al., 1988) is used within a range of validity of $0 < f_l < 0.5$; i.e.,

$$K = K_0 \frac{f_l^3}{(1 - f_l)^2} \tag{9}$$

where K_0 is a porosity constant. In practice, the effect of the source term given by Eq. (7) is as follows. In fully liquid domain ($f_l = 1$), the source term is zero, and has no influence, resulting in momentum conservation equations of the same form as the well-known Navier–Stokes equation. In the elements that are changing phase, it dominates over the transient, convective and diffusive components of the momentum equation, thereby forcing them to imitate the Carman–Kozeny model. In totally solid elements ($f_l = 0$), however, an extremely large magnitude of the term overweighs the effects of all other terms, and forces the velocities to be zero. However, due to inaccuracy of this equation for $f_l > 0.5$, a hybrid model is used for that region (Morvan et al., 1999), as given by:

$$\mu_l = \mu_l^0 \left\{ \frac{A_\mu}{A_\mu - K_1(1 - f_l)} \right\}^2 \tag{10}$$

and

$$K = K_2 K_0 \left[\frac{f_l^3}{(1 - f_l)^2} \right], \quad \text{where } A_\mu = 0.4 \tag{11}$$

Here, K_1 and K_2 are according to the theory of rheology of suspensions reducing the effects of excessive damping action of the Darcy force as:

$$K_1 = 0.5 - \frac{1}{\pi} \arctan\left[100\left(f_l^{cr} - f_l\right)\right] \tag{12}$$

$$K_2 = 0.5 + \frac{1}{\pi} \arctan\left[100\left(f_l^{cr} - f_l\right)\right]^{-4}, \quad \text{where } f_l^{cr} = 0.5 \tag{13}$$

In the above equations, f_l^{cr} can be considered as a critical liquid fraction up to which the Carman–Kozeny equation remains valid. The liquid fraction f_l is calculated as $\Delta H/L$.

In Eq. (7), the enthalpy, H, of a material is expressed as:

$$H = h_s + \Delta H \tag{14}$$

$$h_s = cT \tag{15}$$

where h_s is the sensible heat, and ΔH is the latent heat content. In order to establish a mushy phase change, the latent heat contribution is specified as a function of temperature, T, and the resulting expression is:

$$\Delta H = f(T) \tag{16}$$

Since latent heat is associated with the liquid fraction, f_l, we can write:

$$\begin{aligned} \Delta H = f(T) &= L && \text{for } T \geqslant T_l \\ &= f_l L && \text{for } T_s \leqslant T < T_l \\ &= 0 && \text{for } \quad T < T_s \end{aligned} \tag{17}$$

where T_l is the liquidus temperature at which solid formation begins, T_s is the solidus temperature at which full solidification occurs.

2.1.2. Boundary conditions

At the top surface, we employ a heat balance as follows:

$$-q''(r) + h(T - T_\infty) + \sigma_e \varepsilon\left(T^4 - T_\infty^4\right) = -k \frac{\partial T}{\partial y} \tag{18}$$

where $q''(r)$ is expressed as a Gaussian heat distribution at the top surface, i.e.

$$q''(r) = \frac{Q}{\pi r_q^2} \exp\left(-\frac{r^2}{r_q^2} \right) \tag{19}$$

where Q is the net energy input, which is the product of the laser power and the coupling efficiency, η. In Eq. (19), r_q is the radius of heat input. The top surface is assumed to be flat. Also, at the top surface, the Marangoni convection leads to a shear stress balance expressed as:

$$\tau_{yx} = -\mu\left(\frac{\partial u}{\partial y}\right)_h = \frac{\partial \sigma}{\partial T}\left(\frac{\partial T}{\partial x}\right)_h \tag{20}$$

$$\tau_{yz} = -\mu\left(\frac{\partial w}{\partial y}\right)_h = \frac{\partial \sigma}{\partial T}\left(\frac{\partial T}{\partial z}\right)_h \tag{21}$$

The bottom of the workpiece is assumed to be insulated, while the sides are subjected to heat loss by convection to the ambient.

The governing equations coupled with the initial and boundary conditions are solved using a pressure-based finite volume method according to the SIMPLER algorithm (Patankar, 1980). The nodal latent heat is updated in every iteration in the following manner (Brent et al., 1988; Voller and Prakash, 1987):

$$\left[\Delta H_{\mathrm{p}}\right]_{n+1} = \left[\Delta H_{\mathrm{p}}\right]_{\mathrm{n}} + \frac{a_{\mathrm{p}}}{a_{\mathrm{p}}^{0}}\lambda\left\{\left[h_{\mathrm{p}}\right]_{\mathrm{n}} - F^{-1}(\Delta H_{\mathrm{p}})\right\} \tag{22}$$

where n denotes the iteration level and λ is a relaxation factor. The terms a_{p} and a_{p}^{0} are the nodal-point coefficient and the coefficient associated with the transient part in the discretised energy equation, respectively. In the above formulation, the difference in temperature obtained from the energy equation and that predicted by the phase change considerations is neutralised, leading to a converged solution. It can be noted here that in the present work, we have adopted an alloy phase-change enthalpy-updating scheme, for which an appropriate inverse latent heat function is given by

$$F^{-1}(\Delta H) = cT_{\mathrm{S}} - c(T_{\mathrm{S}} - T_{\mathrm{L}})\left(\frac{\Delta H}{L}\right)^{k_{\mathrm{p}}-1} \tag{23}$$

where T_{S} is the solidus temperature, T_{L} is the liquidus temperature, and k_{p} is the partition coefficient, respectively, corresponding to the nominal composition of the alloy, as dictated by the phase diagram. In this work, we assume a linearized phase diagram corresponding to a dilute binary alloy. A detailed development of the above expression for a non-equilibrium phase change process is given in Chakraborty and Dutta (2001).

2.1.3. Particle tracking

The trajectory of a particle as it is advected within the molten pool is governed by the equation:

$$\frac{\mathrm{d}\vec{x}}{\mathrm{d}t} = \vec{u}(x, y, z, t') \tag{24}$$

where $\vec{x}$ is the position vector of the particle. The velocity components appearing in the above equation are obtained from the fully developed Eulerian velocity field calculated in the first part of the model. It is assumed that the particle moves with the same velocity as that of the fluid. These velocity components in Eq. (24) are numerically integrated in a time marching scheme using a fourth order Runge–Kutta method to obtain the complete particle trajectory. For obtaining the velocity components at any location, a tri-linear interpolation is employed using the velocities at the neighbouring grid points. Simultaneously, the local temperature is interpolated at each and every incremental location in the locus of the particle, to be used for calculations pertaining to particle melting.

2.1.4. Particle-melting module

After introduction of an alloying particle into the meltpool, it is subjected to temperature boundary conditions in accordance with the local temperature of the pool. As the particle is advected within the pool, its temperature boundary condition (surface temperature) also varies according to its location. The particle-melting module solves the transient temperature distribution within the particle (including melting) using a conduction-based analysis. In this model, it is assumed that the alloying particles are spherical in shape and move without any relative velocity with the fluid particles. The energy conservation equation for the particle in a spherical coordinate system is given by:

$$\frac{\partial(\rho T)}{\partial t} = \frac{1}{c_p R^2}\frac{\partial}{\partial R}\left(kR^2\frac{\partial T}{\partial R}\right) - \frac{1}{c_p}\frac{\partial}{\partial t}(\rho\,\Delta H) \tag{25}$$

Eq. (19) is solved using the following boundary conditions:

$$\text{At } r = 0,\ \frac{\partial T}{\partial R} = 0 \quad \text{and} \quad \text{at } R = R_{\mathrm{p}}(t'),$$
$$T_{\mathrm{b}}(t') = T(x, y, z, t') \tag{26}$$

where $R_{\mathrm{p}}(t')$ and $T_{\mathrm{b}}(t')$ are the radius and surface temperature of the particle, respectively, at the specified time t' in the Lagrangian frame. $T(x, y, z, t')$ is the interpolated local temperature in accordance with the current location of the particle in the meltpool.

2.1.5. Species distribution

As the melting particle is tracked, the amount molten in each control volume along its trajectory is recorded. This procedure is repeated for each and every particle introduced on the pool surface. Eventually, a statistical distribution of species mass source inside the pool can be obtained. Using the species mass source, following modified solute transport equation can be solved as:

$$\frac{\partial(\rho C_{\mathrm{l}})}{\partial t} + \nabla\cdot(\rho\vec{u}C_{\mathrm{l}}) = \nabla\cdot(\rho_{\mathrm{l}} f_{\mathrm{l}} D_{\mathrm{l}}\nabla C_{\mathrm{l}}) + k_{\mathrm{p}}C_{\mathrm{l}}\frac{\partial}{\partial t}(\rho f_{\mathrm{l}}) - \frac{\partial(\rho u_{\mathrm{scan}}C_{\mathrm{l}})}{\partial x} + k_{\mathrm{p}}C_{\mathrm{l}}\frac{\partial}{\partial x}(\rho u_{\mathrm{scan}} f_{\mathrm{l}}) + S_{\mathrm{gen}} \tag{27}$$

where, S_{gen} represents a local volumetric species generation term. S_{gen} is calculated by the relation:

$$S_{\mathrm{gen}} = \frac{\dot{m}_{\mathrm{cv}}}{\Delta V} \tag{28}$$

where $\dot{m}_{\mathrm{cv}}$ is the rate at which the species mass melts in a control volume (statistical average for all particles) and ΔV is the volume of the particular computational cell. It can be noted that $\dot{m}_{\mathrm{cv}}$ is obtained as a consequence of particle tracking and particle-melting modules of the present model, in accordance with the local temperature distribution within the particle. Also, it is evident that S_{gen} is not active at all locations in the computational domain. In fact, it is active only at the control volumes where the particles melt. Hence, above formulation of the species source term is a more realistic model of distributed melting than the specification of a mass flux boundary condition at the free surface, as used in previous studies.

The boundary conditions consistent with Eq. (27) at the interfaces are given by:

(a) Melting front:

$$v_n C_l = -D_l \frac{\partial C_l}{\partial y} \tag{29}$$

where v_n is the projection of the traverse speed onto the normal to the solid–liquid boundary.

(b) Solidification front:

$$(1 - k_p) v_n C_l = -D_l \frac{\partial C_l}{\partial y} \tag{30}$$

The modified species conservation equation along with the boundary conditions is solved numerically using a finite volume methodology (Patankar, 1980).

2.2. Numerical simulation

2.2.1. Model validation

The numerical code pertaining to the solution of a three-dimensional set of coupled convection–diffusion equations incorporating phase change considerations is validated by solving a Marangoni convection driven arc welding problem, as described in Dutta et al. (1995). The computer code for the particle-melting module is validated against an analytical solution given in Carslaw and Jaeger (1959) corresponding to a fixed temperature boundary condition. The validated codes are subsequently utilised for the solution of the present problem.

2.2.2. Choice of grid size and time step

In order to resolve the velocity field at the free surface, the vertical gridding at these locations is ascertained by a scaling analysis estimating the thickness of the viscous boundary layer created by surface tension driven flow (Dutta et al., 1995). Such estimations render a value of 3×10^{-6} m as the order of the boundary layer thickness. Accordingly, in the vertical direction, six control volumes are accommodated within that distance, in order to resolve the boundary layer computationally. Below this layer, the grid size is chosen to be 6×10^{-5} m in the vertical direction upto the bottom of the pool and its vicinity. Overall, a $55 \times 40 \times 55$ non-uniform grid is chosen for the domain size of $10 \times 5 \times 5$ mm^3. As an outcome of a comprehensive study, it is revealed that the choice of a finer grid does not alter the accuracy of the solution, for all practical purposes. Regarding the particle-melting module, a grid size of 202×1 is used for a particle size of 12.5 μm radius to capture the interface movement accurately. For solution of the velocity and temperature fields, a variable timestep is employed. The timestep varies from larger values (~0.005 s) during initial conduction-dominated regimes to smaller values (~0.0005 s) after initiation of melting. For a more developed stage of the pool, a coarser timestep (~0.005 s) is used. The choice of timestep for the particle-tracking module is optimised in such a way that the particles do not skip any control volume during the integration. This is ensured by scaling the timestep (Δt) as: $\Delta t \sim \Delta x / u_{max}$, where Δx is the distance between two grid points. It is found that a timestep of the order of 2.5×10^{-6} s is a suitable one in this regard, which is adopted for the particle-melting module also.

2.2.3. Convergence criteria

Convergence in the inner iterations is declared on the basis of relative error of scalar variables to be solved (a tolerance of 10^{-4} is prescribed), as well as on satisfaction of the overall energy balance criteria within a permissible limit of 0.1%.

3. Results and discussion

Case I: The model is first applied to the case of laser surface alloying of aluminium on nickel base metal (which represents the use of a lower melting-point alloy with a higher melting-point base metal). The thermophysical properties, shown in Table 1, are taken from Smithel's HandBook (Brandes, 1983). The process parameters appropriate for the simulated problem are listed in Table 2.

Table 1
List of physical properties

Physical properties	Values	
	Aluminium	Nickel
Constants		
β_T	2.0×10^{-5} K^{-1}	3.0×10^{-5} K^{-1}
T_m	660.0 °C	1452.0 °C
T_{boil}	2520.0 °C	2915.0 °C
L	3.95420×10^5 J/kg	5.9×10^5 J/kg
ρ	2237 kg/m^3	8900 kg/m^3
σ_T	-3.5×10^{-4} N/mK	-3.5×10^{-4} N/mK
Variables		
μ	$1.492 \times 10^{-4} \times \exp(16500/\overline{R}T)$ Nm/s^2	$1.663 \times 10^{-4} \times \exp(50200/\overline{R}T)$ Nm/s^2
k		
$273 \leqslant T \leqslant 373$ K	238.0 W/mK	–
$373 \leqslant T \leqslant 993$ K	231.4 W/mK	–
$T \geqslant 993$ K	109.3 W/mK	–
k		
$273 \leqslant T < 773$ K	–	88.5 W/mK
$773 \leqslant T$	–	62.0 W/mK
c		
$273 \leqslant T < 373$ K	971.0 J/kgK	–
$373 \leqslant T \leqslant 993$ K	1049.2 J/kgK	–
$T \geqslant 993$ K	1212.0 J/kgK	–
c		
$273K \leqslant T < 1173K$	–	452.0 W/mK
$1173K \leqslant T$	–	595.0 W/mK

Table 2
List of process parameters

Process parameters	Values
Q (total heat input)	2400 W
r_q (radius of heat input)	0.9 mm
Radius of nickel particles	35×10^{-6} m
m_f (mass flux added)	2×10^{-5} kg/s
η (efficiency of heat input)	0.22
u_{scan} (laser scanning speed)	0.008 m/s

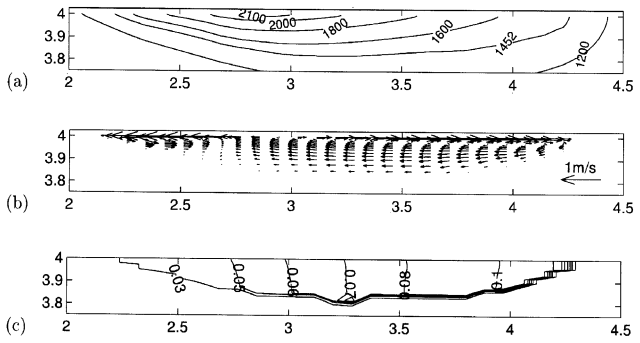

Fig. 3. Results (longitudinal section) for the case of alloying nickel on aluminium substrate (Case I), with $u_{scan} = 0.051$ m/s, power = 2.4 KW, $\eta = 0.22$ and powder feed rate = 0.0156 gm/s. (a) Temperature contours, (b) velocity vector and (c) concentration contours.

Fig. 3 shows the longitudinal section of velocity, temperature, and concentration fields in three different views. A loop of very high velocity is found to exist immediately adjacent to the top surface of the pool. This flow is induced by the surface tension gradient (Marangoni convection) at the surface of the pool. For the present case, the surface tension is a decreasing function of temperature. As a result, liquid metal near the centre of the pool is pulled towards the relatively cooler pool edges, resulting in counter-rotating vortices as shown in Fig. 3. After the hot liquid metal from the pool centre reaches the edge, it turns downwards. Fig. 4 shows the cross-sectional view of the numerically generated pool along with the micrograph of an experimental section. It may be noted from Figs. 3 and 4 that the weld pool is shallow and wide. This is due to the nature of fluid flow, which transports the heat primarily from the centre of the pool to its edges.

Fig. 5 shows the numerical and experimental results of interface composition of the solidified layer. It is observed that the composition of aluminium is maximum at the top surface, and decreases gradually towards the substrate. This can be explained by carefully examining the nature of fluid flow in Fig. 3. Since the aluminium powder introduced at the top surface melts almost instantaneously, the species mass flux is effectively introduced almost entirely at the surface. The Marangoni convection then rapidly transports the molten aluminium towards the edges. As a result, the aluminium composition is likely to be the highest at the top of the solidifying interface (i.e. trailing edge of the pool, as shown in Fig. 3). As we go down along the solidifying interface, there is a progressive dilution effect, and hence the aluminium composition decreases. As observed in Fig. 5, the numerical and experimental results are in good qualitative agreement.

As a separate approach, numerical computations are also executed considering the mass flux of aluminium at the top surface to be in a completely molten state. The Neumann boundary condition (at the top surface) for the latter case can be written as:

$$-\left(D_l \frac{\partial C}{\partial y}\right)_{top} = \dot{m} \tag{31}$$

where $\dot{m}$ is the mass flux of aluminium distributed uniformly over a circular area of radius r_q. In Eq. (31), D_l is the diffusion coefficient of the alloying element in the

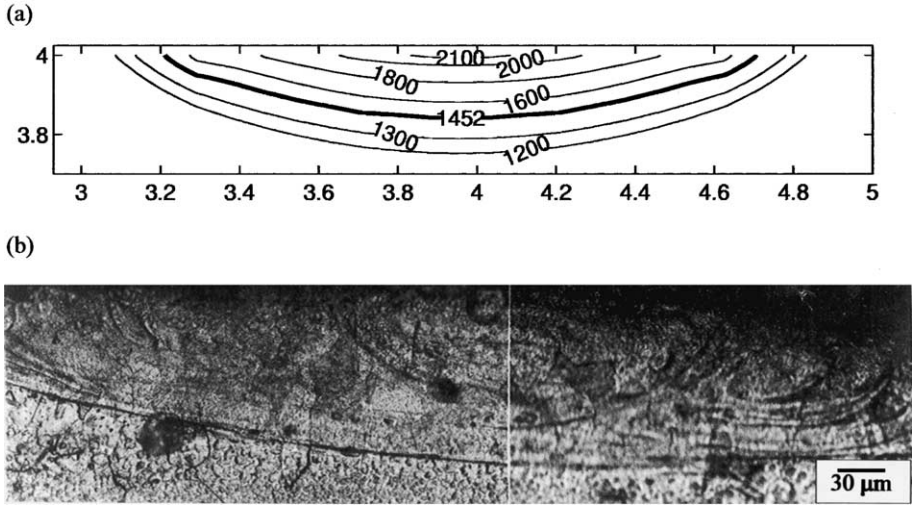

Fig. 4. (a) Cross-sectional view of the numerically generated pool and (b) micrography of an experimental section for the case of laser alloying of Al on Ni (Case I).

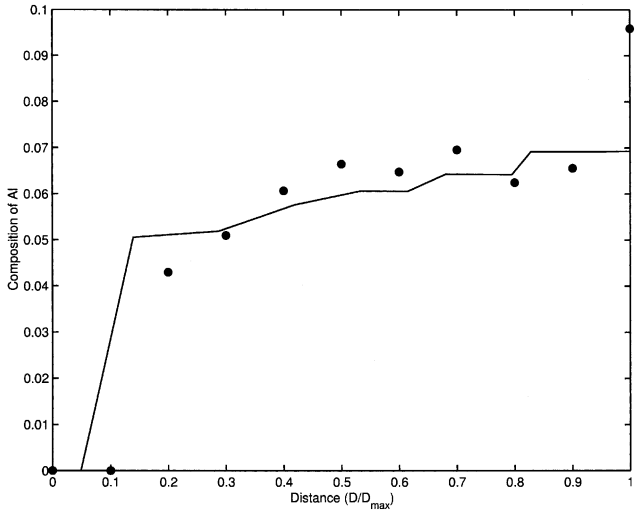

Fig. 5. Composition of solidified layer along the depth of the pool. The solid line is for calculated profile and the dark circles are experimentally determined compositions (Case I).

molten base material. The mass flux $\dot{m}$ is assumed to be uniform and is calculated from the powder feed rate (m_f) as:

$$\dot{m} = \frac{m_{\mathrm{f}}}{\pi r_q^2} \tag{32}$$

It can be noted that the assumption of mass flux boundary condition at the top surface (i.e., equivalently, an instantaneous melting of the alloying element) is appropriate in this case, since the melting point of aluminium is much less compared to that of nickel. A comparison is made between the solidified interface composition obtained from the two procedures (with and without distributed melting approach). The two results (not shown here) match, thus validating the procedure used for distributed melting approach, which we use for the present formulation.

Case II: The model is first applied to the case of laser surface alloying of nickel on aluminium base metal (which represents the use of a lower melting-point alloy with a higher melting-point base metal). Fig. 6 shows the longitudinal section of velocity, temperature, and concentration fields in three different views. As in the previous case, a strong Marangoni convection is found to exist immediately at the top surface of the pool, forming an upper loop. It may be noted from Fig. 6 that the weld pool geometry resembles closely to that predicted by conduction analysis alone. The reason is that liquid aluminium has a low Prandtl number ($Pr \approx 0.004$), and hence the role of convection in the overall transport is not very significant. As a result, convection in the pool does not alter the pool geometry significantly; unlike in the case of a nickel substrate which has a higher Prandtl number. The resulting Peclet number ($u_{\max} \times \mathrm{depth}/\alpha$) for the case of aluminium is also found to be less

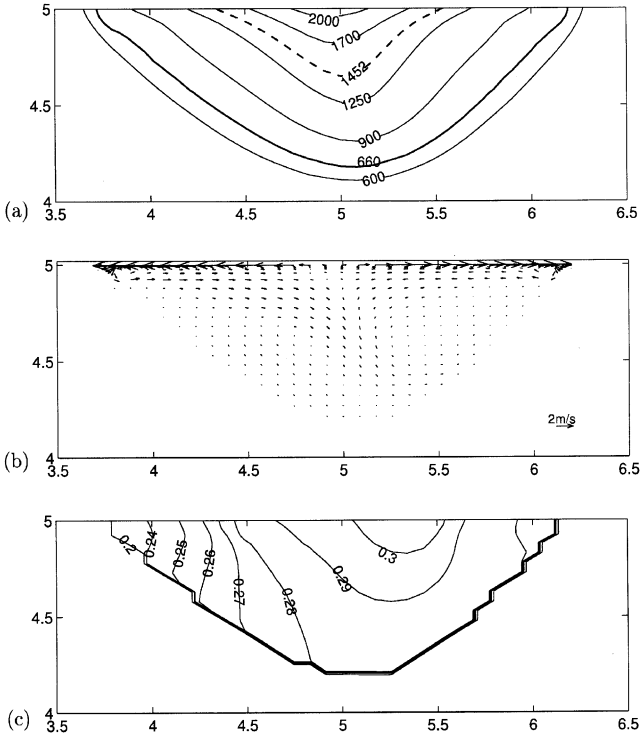

Fig. 6. Results for the case of alloying nickel on aluminium substrate (Case II), with $u_{\mathrm{scan}} = 0.008$ m/s, power = 2.4 kW, $\eta = 22\%$ and powder feed rate = 0.02 gm/s. (a) Temperature, (b) velocity and (c) concentration.

($Pe \approx 61$) compared to that of nickel. The shape of the pool is depicted in Fig. 7, which shows the cross-sectional views of the numerically generated pool along with the micrograph of an experimental section.

It is evident from Fig. 6a that the temperature field can clearly be subdivided into two regions. The first region is the "inner cup" with temperature above 1452 °C (the contour line of 1452 °C corresponds to the melting temperature of the alloying element, nickel). The other region is the "outer cup" for which the temperature is lower than the melting point of the alloying element. Accordingly, if the Ni particles fall within a zone having temperature well above their melting point, they melt almost instantaneously, thereby acting as species sources at the corresponding locations in the molten pool. On the other hand, if the particles fall in the outer cup, they will first be advected radially outwards by the strong Marangoni convection (refer to velocity field in Fig. 6a). Subsequently, these particles can reach zones of temperature greater than their melting point (due to turning effects of the edges of the melt pool) and begin to melt. Instantaneously, the molten species diffuses locally, thereby acting as distributed mass source at that location.

The concentration field obtained inside the molten pool with the distributed source terms is shown in Fig. 6c. In this case, the maximum concentration of nickel is found near the centre of the melt pool surface. The

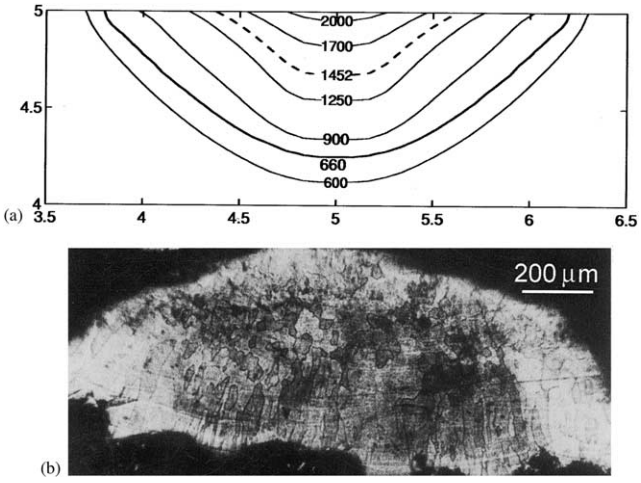

Fig. 7. (a) Cross-sectional view of numerically generated pool and (b) micrography of experimental section for the case of laser surface alloying of Ni on Al (Case II).

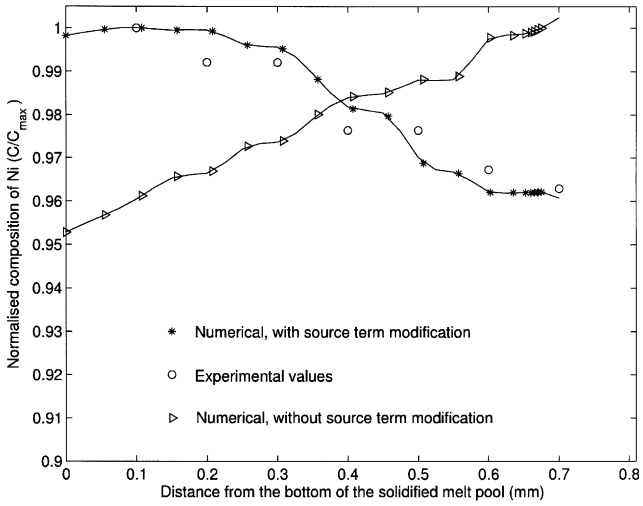

Fig. 8. The concentration variation along the depth of the solidified alloy (Case II).

reason for this can be explained as follows. From the concentration field (Fig. 6c) and the temperature field (Fig. 6a), it may be noticed that the concentration of the species is more on the top surface of the ''inner cup'', where the nickel particles are found to melt almost instantaneously.

Hence, due to the effect of distributed species mass source, the melt pool always experiences a concentrated species flux on the portion of the pool surface within the inner cup, where the temperature is ranging from the melting point of the alloying element to the maximum temperature of the pool (just beneath the laser). The species mass is almost zero in the remaining area of the melt pool surface. This results in a maximum concentration always near the centre of the melt pool surface. However, the effect of dilution and solute rejection also features at the melting and solidification fronts, respectively. This can be visualised by comparing the concentration fields near the solidification front and the melting front, where it is found that the average concentration is more near the solidification front than near the melting front due to solute rejection and dilution, respectively. The final concentration distribution inside the melt pool is determined by the solution of the species conservation equation (21), which includes advection and diffusion in addition to the distribution of species sources described above.

The concentration variation along the depth of the solidified alloy is shown in Fig. 8. From Fig. 8, it is evident that there is a significant difference between predictions by the present model and those using a model without accounting for any distributed melting. The numerical results are also compared with the experimental findings of Balachandran (1998), and it is found that the experimental trend is more accurately captured by the present model than by the previous models. It is important to note that the maximum composition of Ni is found near the bottom of the solidified alloy. This can be attributed as a contribution from the distributed species source terms.

4. Conclusions

A three-dimensional transient numerical model is developed to predict the mass, momentum, heat and species transport during laser surface alloying. The addition of alloying element to the molten pool is represented by a formulation of a distributed species source term in the solute transport equation. It is found that for the case in which the melting point of the alloying material is much lower than that of the substrate (such as Al on Ni), the alloying powder melts almost instantaneously on the pool surface. In this situation, the results are same as that produced by the conventional model which represents the addition of alloying material as a mass flux boundary condition at the pool surface. However, for the opposite case when the melting point of the alloying material is higher than that of the substrate (such as Ni on Al), the present model is found to predict the final species distribution more realistically. For both the above cases, the numerical results predicting the final composition in the solidified alloy are compared with corresponding experimental results, and the agreement is found to be good.

References

Balachandran, R., 1998, Laser surface alloying of nickel on aluminium substrate, M.E. thesis, Indian Institute of Science, Department of Metallurgy, India.

Basu, B., Srinivasan, J., 1988. Numerical study of steady state laser melting problem. Int. J. Heat Mass Transfer 11, 2331–2338.

Brandes, E.A., 1983. Smithells metals reference book. Butterworths and Co. Ltd, London.

Brent, A.D., Voller, V.R., Reid, K.J., 1988. Enthalpy-porosity technique for modelling convection-diffusion phase change: application to the melting of a pure metal. Numer. Heat Transfer A 13, 297–318.

Carslaw, H.S., Jaeger, J.C., 1959. Conduction of Heat in solids. Oxford University Press, UK.

Chakraborty, S., Dutta, P., 2001. A generalised formulation for evaluation of latent heat functions in enthalpy-based macroscopic models for convection-diffusion phase change processes. Metall. Mater. Trans. B 32B, 562–564.

Chan, C.L., Mazumdar, J., Chen, M.M., 1984. Two dimensional transient model for convection in laser melted pool. Metall. Trans. A 15A, 2175–2184.

Chan, C.L., Mazumdar, J., Chen, M.M., 1987. Three dimensional axisymmetric model for convection in laser melted pools. Mater. Sci. Technol. 3, 306–311.

Chan, C.L., Mazumdar, J., Chen, M.M., 1988. Effect of surface tension gradient driven convection in a laser melt pool: three dimensional perturbation model. J. Appl. Phys. 64 (11), 6166–6175.

Chen, J.C., Huang, Y.C., 1990. Thermocapillary flow of surface melting due to a moving heat flux. Int. J. Heat Mass Transfer 34 (3), 663–671.

Dutta, P., Joshi, J., Janaswami, R., 1995. Thermal modeling of GTAW process with non axisymmetric boundary conditions. Numer. Heat Transfer A 27, 499–518.

He, X., Mordike, B.L., Pirch, N., Kreutz, E.W., 1995. Laser surface alloying of metallic materials. Lasers Eng. 4, 291–316.

Kou, S., Wang, Y.H., 1986. Three dimensional convection in laser melted pools. Metall. Trans. A 17A, 2265–2270.

Morvan, M., Ganaoui, E., Bonboux, P., 1999. Numerical simulation of a 2-D crystal growth problem in vertical Bridgman–Stockbarger furnace: latent heat effect and crystal-melt interface morphology. Int. J. Heat Mass Transfer 42, 573–579.

Patankar, S.V., 1980. Numerical Heat Transfer and Fluid Flow. Hemisphere, New York, NY.

Voller, V.R., Prakash, C., 1987. A fixed grid numerical modeling methodology for convection/diffusion phase change problems. Int. J. Heat Mass Transfer 30, 1709–1719.